NANO LETTERS

pubs.acs.org/NanoLett

Letter

Electrified *Operando*-Freezing of Electrocatalytic CO_2 Reduction Cells for Cryogenic Electron Microscopy

Yanbin Li,[¶] Yunzhi Liu,[¶] Zewen Zhang, Weijiang Zhou, Jinwei Xu, Yusheng Ye, Yucan Peng, Xin Xiao, Wah Chiu, Robert Sinclair, Yuzhang Li,* and Yi Cui*

Cite This: *Nano Lett.* 2024, 24, 10409−10417

Read Online

ACCESS | Metrics & More | Article Recommendations | Supporting Information

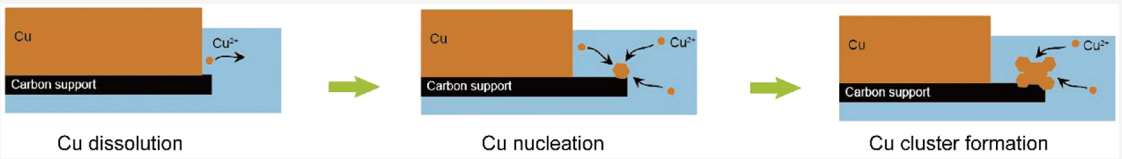

ABSTRACT: The ability to freeze and stabilize reaction intermediates in their metastable states and obtain their structural and chemical information with high spatial resolution is critical to advance materials technologies such as catalysis and batteries. Here, we develop an electrified *operando*-freezing methodology to preserve these metastable states under electrochemical reaction conditions for cryogenic electron microscopy (cryo-EM) imaging and spectroscopy. Using Cu catalysts for CO_2 reduction as a model system, we observe restructuring of the Cu catalyst in a CO_2 atmosphere while the same catalyst remains intact in air at the nanometer scale. Furthermore, we discover the existence of a single valence Cu (1+) state and C−O bonding at the electrified liquid−solid interface of the *operando*-frozen samples, which are key reaction intermediates that traditional *ex situ* measurements fail to detect. This work highlights our novel technique to study the local structure and chemistry of electrified liquid−solid interfaces, with broad impact beyond catalysis.

KEYWORDS: *Catalysis, CO_2 reduction, Cryogenic Electron Microscopy, Operando-Freezing, Electrified Liquid−Solid Interfaces*

Electrochemical energy technologies, such as batteries and electrocatalysts, are essential for decarbonizing the global economy and enabling clean energy conversion and storage for a sustainable future.[1−10] Underlying these technologies are multiple interfacial reaction intermediate states like ion solvation/desolvation, surface adsorption, dissolution/coalescence of active materials and oxidation/reduction of active materials surfaces.[11−17] However, these intermediate structural and compositional changes are extremely difficult to probe directly under operating conditions with high spatial resolution due to their short lifetime. Previously, ultrafast spectroscopy and X-ray diffraction have been used to study the intermediate states in batteries and electrocatalysis,[18,19] but these approaches are largely limited to capturing ensemble information and are not able to identify local heterogeneities.

The rapid and recent progress in cryogenic electron microscopy (cryoEM) for physical sciences has started to offer researchers new tools and methods to probe many otherwise inaccessible components and phenomena in electrochemical energy science.[20,21] Specifically, weakly bonded and reactive materials, interfaces and phases that typically degrade under high energy electron-beam irradiation and environmental exposure can be protected and stabilized by cryogenic methods for structural and chemical analysis with atomic resolution.[22−28] In principle, capturing metastable reaction intermediates is possible by rapid freezing to kinetically trap them at low temperature, preventing any relaxation back to equilibrium. Indeed, previous time-resolved cryoEM studies in biosciences[29] have successfully demonstrated the freezing and preservation of intermediate states during chemical reaction. Thus, it is important to develop cryoEM techniques to freeze the structure of an inherently unstable and evolving electrochemical system in its operating and metastable state while applying an external stimulus (such as voltage and light), which will further permit the *operando* high-resolution characterization of reaction intermediates. Here, we report an electrified *operando*-freezing technique in which we designed a microelectrochemical cell (micro-EC) to enable rapid plunge-freezing of the full device while applying voltage. To demonstrate the utility of this new technique, we focus on studying the electrochemical carbon dioxide reduction reaction (CO_2RR) using evaporated metallic copper as an electrocatalyst.

Copper is one of the few metallic catalysts that can electrochemically reduce CO_2 to generate hydrocarbons and alcohols with decent efficiency.[30] In particular, oxide-derived Cu catalysts have been reported to have higher selectivity toward

Received: August 9, 2023
Revised: August 8, 2024
Accepted: August 9, 2024
Published: August 19, 2024

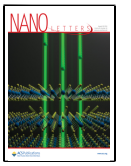

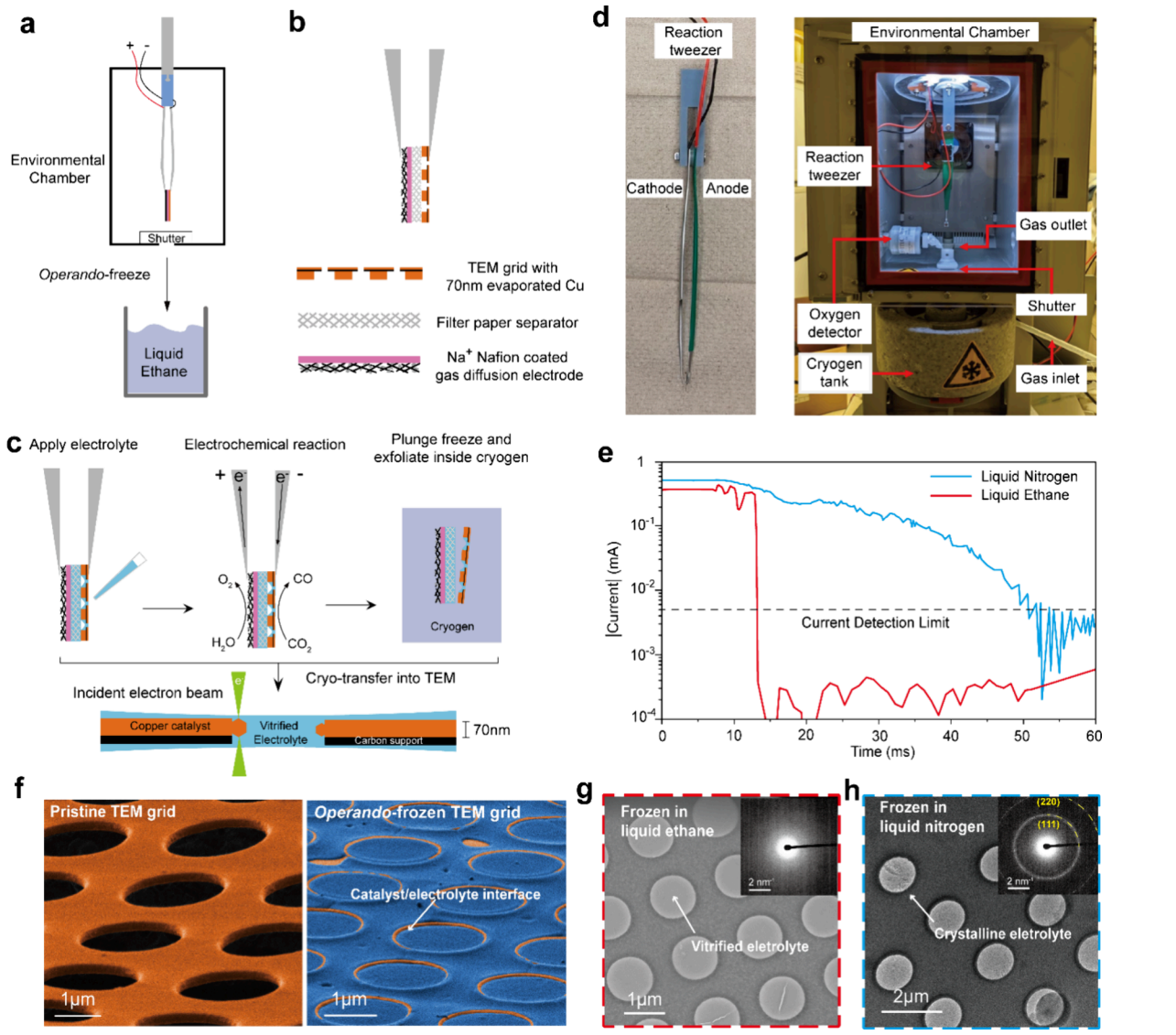

Figure 1. | Electrified *operando*-freeze of electrocatalytic CO_2 reduction reaction (CO_2RR). (a-b) Schematic of *operando*-freezing apparatus. (a) Microelectrochemical cell (micro-EC) runs CO_2RR inside an environmental chamber (100% humidity) and is then plunged into liquid ethane while applying voltage. (b) The micro-EC consists of a Cu-coated TEM grid (working electrode), filter paper separator, and gas diffusion electrode (GDE, counter electrode) coated with Na^+ form Nafion membrane. (c) Schematic of sample preparation process. After *operando*-freezing, the TEM grid is exfoliated inside cryogen and cryo-transferred into TEM column using Gatan Cryo-transfer holder. (d) Digital image of reaction tweezer and environmental chamber. (e) Current profile of micro-EC frozen in liquid ethane (red) and liquid nitrogen (blue). The current drops below detection limit within 5 ms for liquid ethane cryogen, while it takes 45 ms for liquid nitrogen cryogen. Dashed black line indicates the current change detection limit. (f) Colored cryo-SEM images of pristine TEM grid and *operando*-frozen TEM grid with contrast from secondary electron. Orange and blue regions represent areas of Cu and frozen electrolyte, respectively. (g-h) Low magnification bright field cryo-EM images and SAED pattern (inset) of samples frozen in (g) liquid ethane and (h) liquid nitrogen. SAED patterns are taken on the frozen electrolyte inside the holes. (g) SAED pattern has no diffraction ring suggesting the successful vitrification of electrolyte. (h) The diffraction rings fit ice (111) and (200) *d*-spacings suggesting the existence of polycrystalline ice due to slower cooling speed of liquid nitrogen.[42]

C_2+ products and improved stability.[31] Disagreement in the literature still exists as to why such catalysts perform well; both subsurface oxygen[32] and higher oxidized states of Cu have been argued to be the reason for improved performance.[33] Furthermore, a theoretical study has attributed the unique ability of Cu in CO_2RR to the fact that it is the only metal that has a negative adsorption energy for adsorbed CO, an important CO_2RR intermediate, but positive adsorption energy for adsorbed H, an intermediate in the competing and unwanted hydrogen evolution reaction (HER).[34] The current understanding of Cu electrochemical CO_2RR is largely limited to ensemble measurements such as X-ray diffraction,[5,19] broad-beam surface-sensitive techniques such as X-ray photoelectron spectroscopy and secondary-ion mass spectrometry,[35,36] or *ex situ* transmission electron microscopy (TEM).[37] Although, *in situ* liquid cell TEM[38] has been used to follow the dynamic structural changes of Cu nanocatalysts, the accumulation of large electron doses during prolonged image acquisition limits such studies to beam-stable species and liquid electrolyte.[39]

Indeed, understanding the effect of electron beam damage on a frozen sample is critical to avoid any artifacts during cryo-EM imaging and spectroscopy.[39] Here, using the electrified *operando*-freezing technique developed in this work, we first carefully characterize the effects of beam damage on our vitrified

https://doi.org/10.1021/acs.nanolett.3c03000
Nano Lett. 2024, 24, 10409−10417

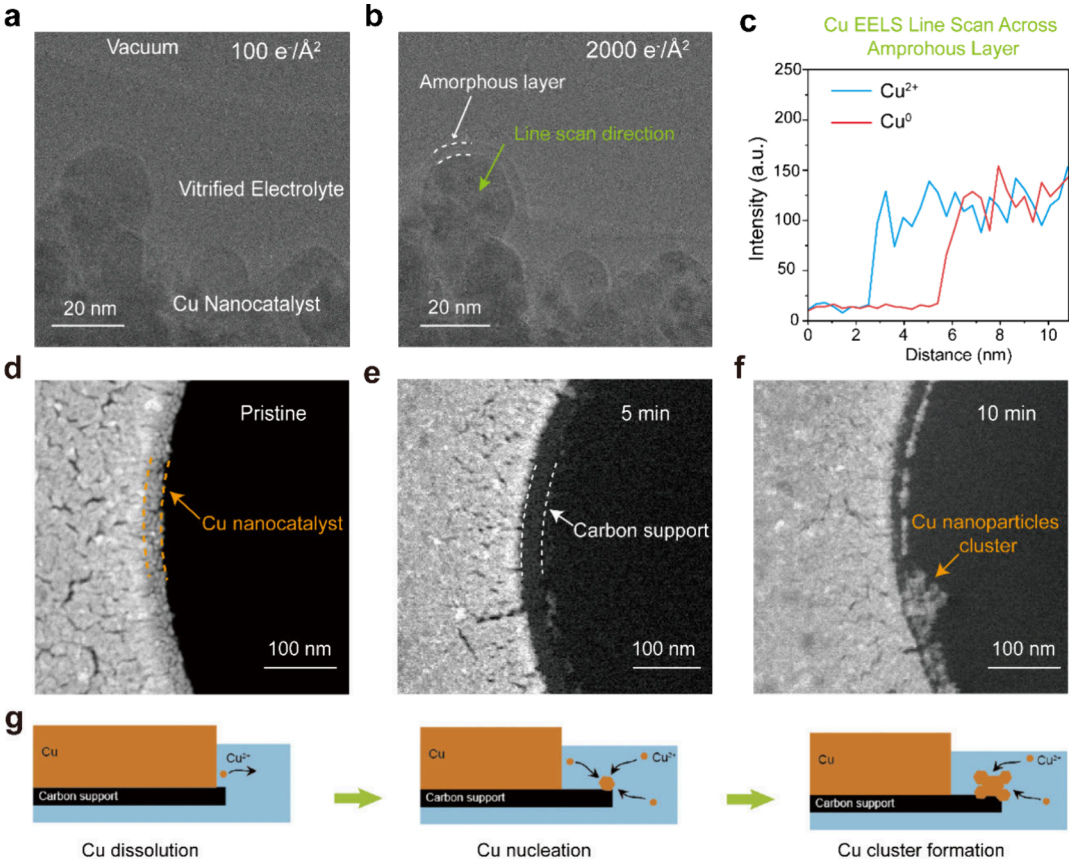

Figure 2. | (a-c) High mag cryo-EM images of *operando*-frozen sample and radiation damage study. CryoEM images of *operando*-frozen sample with cumulative electron exposure (a) 100 $e^-/Å^2$ and (b) 2000 $e^-/Å^2$. An amorphous layer formed on the surface of Cu nanocatalyst, after 2000 $e^-/Å^2$ cumulative electron exposure. (c) Line profile of Cu^{2+} (blue) and Cu^0 (red) EELS L_3 peak signal intensity along the line scan direction showed in (b) green line (from the electrolyte into the copper), which suggests the formation of Cu^{2+}-rich shell on Cu nanocatalyst after e-beam radiation damage. (d-f) Morphological evolution of Cu nanocatalysts during electrochemical CO_2RR. Cryo-STEM-ADF images of (d) pristine and *operando*-frozen samples after running CO_2RR for (e) 5 and (f) 10 min. No Cu nanoclusters (2−4 nm) from fragmentation were observed throughout the process. (g) Schematic of Cu dissolution and redeposition process during electrochemical CO_2RR: Cu nanocatalysts around the edge first dissolved into electrolyte and expose carbon support underneath it; Later, Cu nanoparticles start to form clusters (~20 nm) on the edge of carbon support. Electrolyte: 0.1 M CO_2-saturated $KHCO_3$. External voltage: −2.5 V.

samples and indeed observe a thin Cu^{2+}-rich surface layer after prolonged e-beam exposure by scanning transmission electron microscopy and electron energy loss spectroscopy (STEM-EELS). We hypothesize that these Cu^{2+} species originate from Cu dissolution into the electrolyte during the CO_2RR that we capture during *operando* freezing. Furthermore, using a minimum STEM probe current to greatly reduce any effects of the electron beam, we discovered the existence of single valence Cu^+ state and C−O bonding at the catalyst-electrolyte interface of the *operando*-frozen sample. These results have significant implications for the understanding of the intermediate states of Cu nanocatalysts under electrochemical reaction conditions.

Figure 1a−c shows a schematic of the apparatus and the process to study the electrified liquid−solid interface. To facilitate rapid temperature quenching, we first developed a micro electrochemical cell (micro-EC) architecture that consists of a filter paper separator sandwiched by a Cu-coated TEM grid (working electrode) and a gas diffusion electrode (GDE, counter electrode) coated with Na^+ form Nafion membrane (Figure 1b). We use Na^+ form Nafion membrane to minimize the pH change at the Cu TEM grid side during CO_2RR and prevent oxygen generated at the counter electrode diffusing to the Cu side. We designed a reaction tweezer with two electrically isolated tips that function as electrodes to contact working and counter electrodes of micro-EC respectively (Figures 1c,d).

We then mounted the reaction tweezer inside an airtight environmental chamber (Figure 1d). Since the surface of Cu nanocatalysts tends to rapidly oxidize under air exposure,[33] the oxygen level inside the chamber is monitored and maintained below 10 ppm during CO_2RR. A small volume (~1 μL) of liquid electrolyte (0.1 M $KHCO_3$ or 0.1 M Na_2SO_4) added to the separator completes the micro-EC circuit. The filter paper separator absorbs extra electrolyte to form a thin layer of electrolyte on the TEM grid. To minimize electrolyte evaporation during CO_2RR, the relative humidity inside the environmental chamber is maintained at 100%. Compared with a micro-EC running outside the chamber, the CO_2RR current of micro-EC inside the environmental chamber remains stable for more than 10 min (Supplementary Figure 1). During the CO_2RR the environmental chamber is filled with a CO_2/Argon (roughly 20% CO_2 and 80% Argon) mixture gas at 1 atm pressure (Supplementary Method). Compared with a micro-EC running in an air atmosphere, the current of micro-EC in a CO_2/Ar atmosphere is 50% higher indicating the onset of the CO_2RR (Supplementary Figure 1). While applying external voltage, the micro-EC is plunge-frozen into liquid ethane cryogen (−182 °C) and the current drops below our detection limit (5 μA)

https://doi.org/10.1021/acs.nanolett.3c03000
Nano Lett. 2024, 24, 10409−10417

within 5 ms (Figure 1e red). As illustrated in Figure 1c, the micro-EC was then exfoliated while immersed in the cryogen, and the working electrode was cryo-transferred[22] into a TEM column (operating at 300 kV) for cryo-EM imaging using a direct-detection electron-counting camera (DDEC). The samples are always kept at the liquid nitrogen temperature during the transfer process.

Due to the electrowetting[40] effect, liquid electrolyte will uniformly cover the surface of Cu nanocatalysts when applying voltage during electrochemical CO_2RR. This electrowetting phenomenon was clearly observed in our experiment (Supplementary Video 1). Figure 1f shows cryoscanning electron microscopy (cryo-SEM) images of pristine and *operando*-frozen TEM grids annotated as orange and blue areas representing Cu and electrolyte, respectively. A clear catalyst-electrolyte interface is observed around the edge of each hole, which corresponds to an electrified liquid−solid interface during CO_2RR. The amorphous contrast and selected area electron diffraction (SAED) pattern, in the TEM, of electrolyte film frozen in liquid ethane confirms the successful vitrification process, without generating any experimental artifacts such as solvent crystallization or salt precipitation (Figure 1g).[41] We attribute the formation of an electron-transparent vitreous electrolyte layer to both the electrowetting effect during electrocatalytic CO_2RR and the use of liquid ethane as cryogen for fast freezing (5 ms). For comparison, liquid nitrogen was used as an alternative cryogen which has a much slower freezing rate (~45 ms as shown in Figure 1e blue), resulting in the crystallization and phase separation of solvent and salt[42] (Figure 1h).

Electron beam induced radiation damage is a fundamental factor that limits the resolution of frozen-hydrated specimens.[43] Furthermore, radiation damage upon the cumulative electron dose has been reported in various e-beam sensitive material systems even at liquid nitrogen temperature.[20] To avoid any artifacts in our cryo-EM and cryo-STEM-EELS studies, we first investigated the effects of the cumulative electron dose on structural and compositional changes in the *operando*-frozen sample. With the aid of the electron counting mode of DDEC, we measure the electron dose rate during imaging to be at 20 $e^{-}Å^{-2}s^{-1}$. Figure 2a,b are successive HRTEM images of the *operando*-frozen sample with increasing cumulative electron dose (100 and 2000 $e^{-}/Å^{2}$). After 2000 $e^{-}/Å^{2}$ of cumulative electron exposure, a thin amorphous layer (~3 nm) appears on the surface of the Cu nanocatalyst (Figure 2b). The thickness of this amorphous layer remains the same under extended e-beam illumination, indicating its stability to further radiation damage (Supplementary Figure 2). We then used cryo-STEM-EELS to examine the surface of an e-beam damaged Cu nanocatalyst to understand the chemical composition of this amorphous layer (Figure 2b,c). The normalized intensity of the Cu^{2+} L_3 peak and Cu^{0} L_3 peak (Supplementary Figure 3) across the line scan region are plotted in Figure 2c. The onset position difference between Cu^{2+} L_3 (blue line) and Cu^{0} L_3 (red line) signal is consistent with the thickness of the amorphous layer measured from cryoEM image (~3 nm), which revealed a core−shell structure with Cu^{2+} rich amorphous shell and crystalline Cu^{0} core. This result indicates that e-beam damage will deposit Cu^{2+} species (likely from the liquid phase due to Cu dissolution during the CO_2RR) on the surface of the *operando*-frozen Cu nanocatalyst. Thus, in our cryo-EM studies below, we minimize the total electron dose used in cryoEM and cryo-STEM accordingly to avoid the formation of Cu^{2+} species on the nanocatalyst surface (Supplementary Method).

The morphological evolution of Cu nanocatalysts (see below) during electrolysis has been reported to have various effects on their selectivity.[44−46] A previous *ex situ* TEM study[47] by transferring Cu nanocatalysts onto TEM grid after electrochemical reaction show that the predominant degradation pathway is a potential-induced fragmentation into 2−4 nm size Cu nanoclusters. However, the air exposure during transfer process can lead to surface oxidation due to its high reactivity.[44] Using our *operando*-freezing and cryo-transfer procedures, we examined the morphology evolution of Cu nanocatalysts during electrochemical CO_2RR without any air exposure.

Figure 2d−f are cryo-STEM-ADF images of pristine (Cu alone without electrolyte) and *operando*-frozen samples after conducting CO_2RR in 0.1 M $KHCO_3$ under −2.5 V external voltage for 5 and 10 min, respectively. Before operando-freezing, the as-evaporated pristine Cu nanocatalysts exist as random shape particles with a 20−40 nm diameter at the edge of the carbon support hole (Figure 2d). Compared to the pristine sample, Cu nanocatalysts disappear around the edge after 5 min (Figure 2e). No Cu nanoclusters from fragmentation were observed at this initial stage, which is different from a previous *ex situ* TEM study.[47] As the reaction time extended to 10 min, clusters of Cu nanoparticles started to form around the edge (Figure 2f). Instead of a potential-induced fragmentation process as reported in previous *ex situ* study,[47] we observed the morphological evolution of Cu nanocatalysts through a dissolution/redeposition pathway as schematically shown in Figure 2g. Initially, Cu nanocatalysts dissolve during the CO_2RR and expose the carbon support underneath them (Figure 2e). As the Cu^{2+} concentration in the electrolyte increases from increasing Cu dissolution, metallic Cu clusters likely start to nucleate at the carbon support edges under the negative applied potential.

Based on this result, we hypothesize that the Cu^{2+} amorphous shell (Supplementary Figure 3) observed in the electron beam dose test (Figure 2b) is induced from prolonged e-beam exposure, which decomposes the water molecule[39] and forms copper(II) compounds by bonding with the Cu^{2+} ions in electrolyte generated from Cu dissolution during CO_2RR. Interestingly, a previous *in situ* liquid cell TEM study observed no changes in the nanostructure morphology after 500s of CO_2RR.[38] Since liquid cell experiments require a CO_2-saturated electrolyte as the carbon source for the CO_2RR, the gas phase CO_2 concentration at the catalyst-electrolyte interface is lower compared with our experimental conditions.

To confirm the influence of gas phase CO_2 on the Cu dissolution during CO_2RR, we conducted an experiment in air atmosphere (100% humidity) in the absence of CO_2 gas and observed that Cu nanocatalysts remain intact even after 10 min of electrolysis (Supplementary Figure 4). Thus, we hypothesize that the existence of gas phase CO_2 molecules at the catalyst/electrolyte interface lead to the faster Cu dissolution in our study, compared with previous *in situ* liquid cell studies that lack CO_2 gas. This result could have important implications for understanding the stability of Cu nanocatalysts in GDE.

In addition to studying the morphological evolution of the Cu catalyst during the CO_2RR, our *operando*-freezing technique allows us to kinetically trap and capture metastable intermediates at the electrified liquid−solid interface that only exist under reaction conditions. Specifically, we leverage cryo-STEM EELS to investigate the chemistry at this interface, revealing the oxidation state of surface Cu in the solid state and the adsorbed intermediates species in the liquid state.

https://doi.org/10.1021/acs.nanolett.3c03000
Nano Lett. 2024, 24, 10409−10417

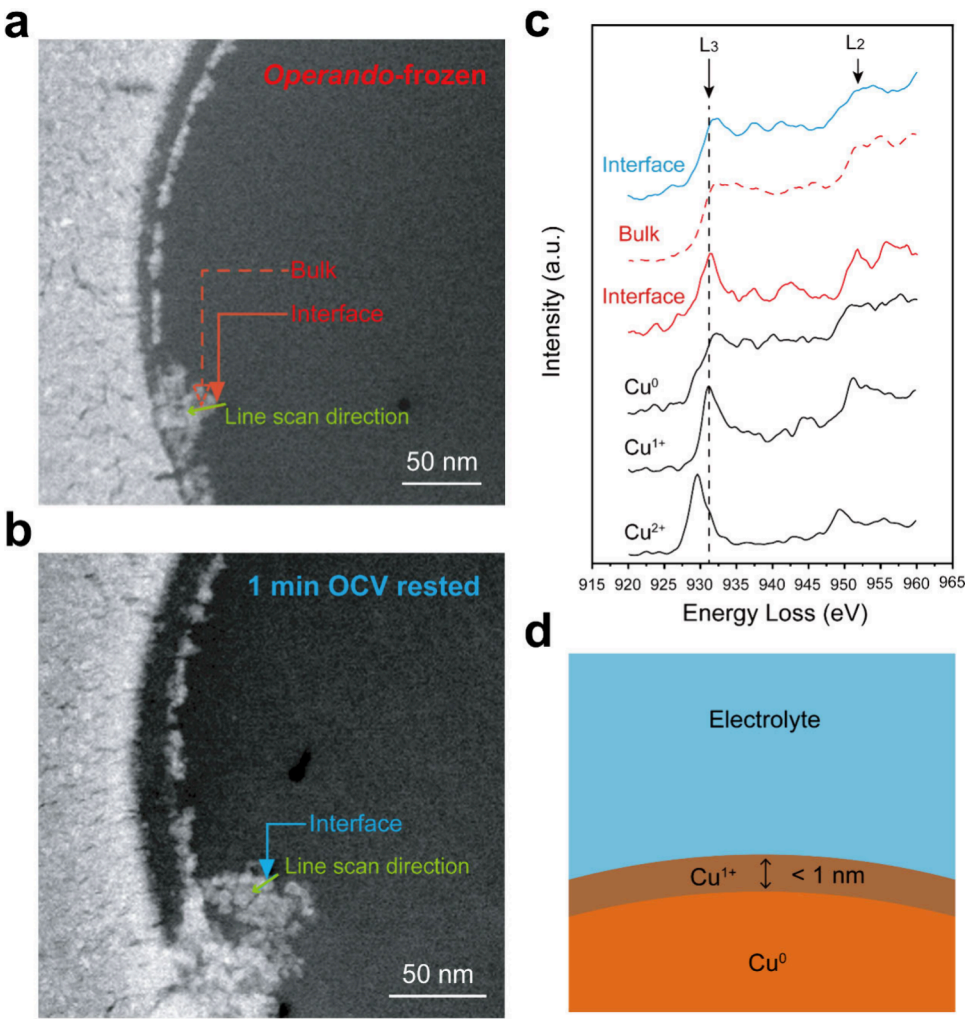

Figure 3. | Analysis of intermediate Copper oxidation state across catalyst-electrolyte interface. Cryo-STEM-ADF images of (a) *operando*-frozen sample:10 min CO_2RR and (b) control sample: biased for 9 min then rested at OCV for 1 min before freezing. (c) Copper EELS signal. The spectra was taken from individual points as indicated in A and B from the line scan and reference samples (Supplementary Method). Key features in EELS spectrum (L_3 peak position and L_3/L_2 height ratio) are summarized in Table 1. Solid and dashed red curves suggest the existence of Cu (1+) state at the electrified liquid−solid interface. Solid red and blue curves confirm that Cu (1+) is intermediate state. Vertical dashed black line marks Cu^{1+} L_3 peak position from reference spectrum at 931.25 eV. (d) Schematic of Cu (0) and Cu (1+) core−shell structure formed during CO_2RR based on EELS line scan results. The thickness of Cu (1+) layer is less than 1 nm. Electrolyte used in (a−c): 0.1 M CO_2-saturated $KHCO_3$. External voltage: −2.5 V.

To investigate the Cu nanocatalyst surface under reaction conditions, we performed *operando*-freezing on our micro-EC during the CO_2RR in a 0.1 M CO_2-saturated $KHCO_3$ electrolyte solution in a CO_2/Ar-filled environmental chamber at 1 atm pressure (20% CO_2 and 80% Argon). Figure 3a shows a cryo-STEM-ADF image of the frozen sample after 10 min operation. We distinguish between the bulk and surface Cu oxidation states using cryo-STEM EELS to perform a line scan across the catalyst-electrolyte interface (green line in Figure 3a) of the Cu L-edge signal. We carefully minimize the electron beam dose to avoid any potential beam-induced artifacts as we described previously. Due to the capability of our equipment, the cryo-STEM-EELS line scan resolution in this experiment is limited to 0.5 nm to avoid any radiation damage from the e-beam. Table 1 summarizes the key features (L_3 peak position and L_3/L_2 peak height ratio) of the Cu L-edge EELS spectrum captured at different locations and in different samples. Interestingly, the Cu L-edge spectra at the Cu surface (solid red line in Figure 3a,c) and bulk (dashed red line in Figure 3a,c) are distinct from each other. To identify the Cu oxidation states in each EELS spectrum, we captured EELS spectra on reference samples (Supplementary Method) and summarize the results in Figure 3c (black curves) and Table 1. Based on the L_3 peak position and L_3/L_2 peak ratio of reference EELS spectra (solid black curves in Figure 3c and Table 1), we find that the Cu surface (solid red line in Figure 3c) spectrum corresponds to the Cu 1+ oxidation state with an L_3 peak at 931.5 eV (Cu 1+ reference: 931.25 eV) and L_3/L_2 peak ratio of 0.94 (Cu 1+ reference: 0.90) whereas the bulk (dashed red line in Figure 3c) spectrum corresponds to the metallic Cu 0 oxidation state with an L_3 peak at 932.25 eV (Cu 0

Table 1. EELS Spectrum Key Features in Figure 3c

EELS spectrum region	L_3 peak position	L_3/L_2 height ratio
Interface (Operando-frozen)	931.5 eV	0.94
Bulk (Operando-frozen)	932.25 eV	0.69
Interface (1 min OCV rested)	932.25 eV	0.71
Cu^0 ref. (evaporated Cu)	932.25 eV	0.74
Cu^{1+} ref. (copper(I) acetate)	931.25 eV	0.90
Cu^{2+} ref. (copper(II) acetate)	929.5 eV	1.77

https://doi.org/10.1021/acs.nanolett.3c03000
Nano Lett. 2024, 24, 10409−10417

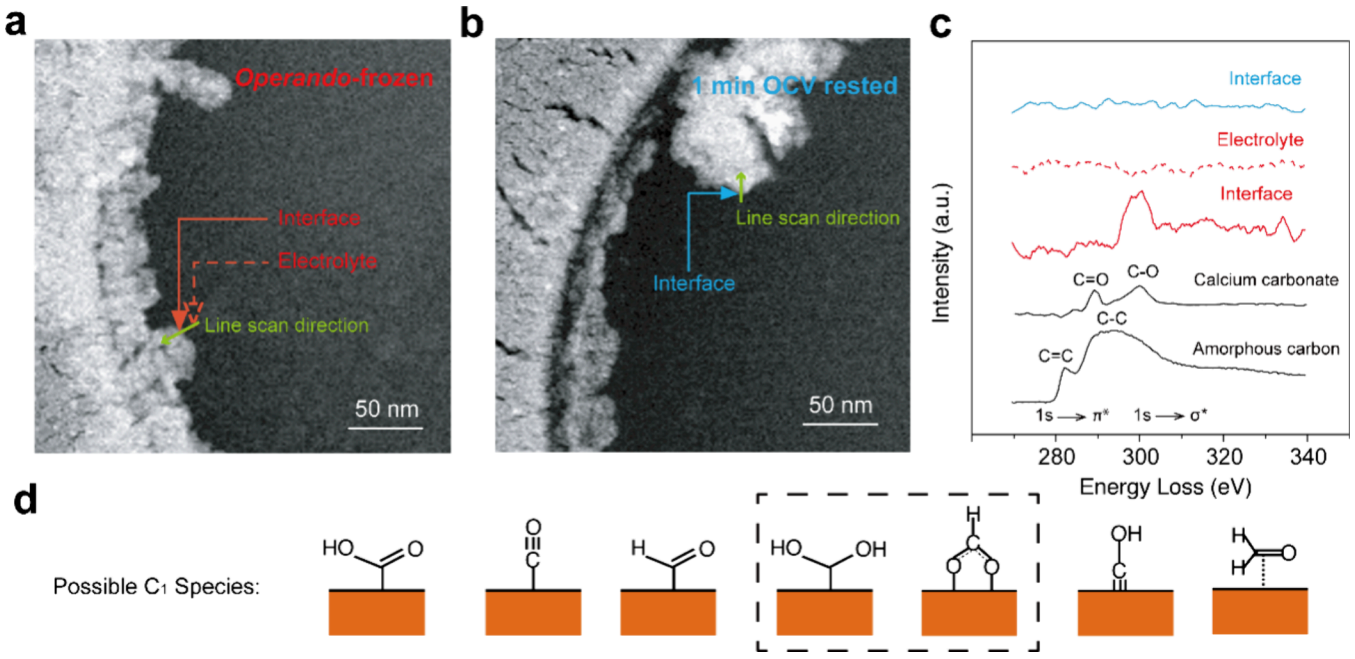

Figure 4. | Analysis of intermediate Carbon bonding states across catalyst-electrolyte interface. Cryo-STEM-ADF images of (a) *operando*-frozen sample: 10 min CO_2RR and (b) control sample: biased for 9 min then rested at open circuit voltage (OCV) for 1 min before freezing. (c) Carbon EELS signal from line scan region in (a and b). Solid and dashed red curves suggest the existence of C−O bond at the electrified liquid−solid interface. Solid blue and red curves confirm that C−O bond exists in intermediate state. (d) Schematic of C_1 intermediate species on the Cu catalyst surface during CO_2RR based on previous studies. The 4th and 5th configurations are possible intermediate species observed in our system which have been both recognized as important intermediate states to produce liquid fuels such as CH_3OH (fourth configuration) and formic acid (fifth configuration) in Cu-catalyzed CO_2RR.[49,50] Electrolyte used in (a-c): 0.1 M N_2-saturated Na_2SO_4. External voltage: −2.5 V.

reference: 932.25 eV) and L_3/L_2 peak ratio of 0.69 (Cu 0 reference: 0.74). The Cu1+ signal persists on the catalyst surface for less than 1 nm from it.

Furthermore, we conducted a control experiment to rule out the possible origin of the Cu 1+ signal from a surface native oxide layer. This control also performed CO_2RR under the exact same conditions but was frozen after the micro-EC was rested for 1 min at open circuit voltage (OCV) with no applied bias, allowing metastable states during reaction to relax back to their equilibrium state (Figure 3b). Notably, the Cu surface (solid blue curve in Figure 3c) spectrum of the control sample corresponds to metallic Cu 0 state with an L_3 peak at 932.25 eV (Cu 0 reference: 932.25 eV) and L_3/L_2 peak ratio of 0.71 (Cu 0 reference: 0.74). The lack of the Cu 1+ signal highlights the importance of our technique in detecting the intermediate state of Cu during electrochemical reactions, which would be missed when carrying out traditional *ex situ* characterization since the Cu surface tends to rapidly oxidize to Cu_2O under air exposure.[33] Indeed, previous *in situ* X-ray absorption spectroscopy studies have observed the existence of Cu+ species in an oxide-derived Cu catalyst at highly negative CO_2RR potentials, however the concern is that Cu+ signal originates from residual CuOx.[33,48] Here, we report that Cu 1+ is also the active state for an oxide-free metallic Cu catalyst during the CO_2RR.

We now examine the frozen (vitrified) liquid phase of the electrified liquid−solid interface. The adsorbed intermediate species at the liquid−solid interface is likely to be primarily carbon-based, which can be revealed using cryo-STEM EELS. To eliminate carbon signal contributions from the carbonate electrolyte, we performed *operando*-freezing of our micro-EC during CO_2RR using a 0.1 M N_2-saturated Na_2SO_4 electrolyte solution (a common electrolyte for CO_2RR) in a CO_2/Ar-filled environmental chamber at 1 atm pressure (20% CO_2 and 80% Argon). Specifically, this electrolyte was selected so that any carbon spectroscopic signal detected by cryo-STEM EELS comes from only electrochemically reduced CO_2 in the surrounding atmosphere.

Figure 4a shows a cryo-STEM-ADF image of the operando-frozen sample after 10 min reaction. We used cryo-STEM EELS to perform a line scan of the carbon K-edge at the liquid−solid interface (green lines in Figure 4a,b). Reference carbon EELS spectrum[49] are also plotted in Figure 4c for comparison. No carbon signal is detected in the bulk liquid (dashed red curve in Figure 4c). We attribute this to the carbon-free electrolyte and insufficient reaction time to accumulate enough liquid phase CO_2RR products for the EELS measurement. In contrast, we do see a clear carbon signal at the interface between the Cu surface and the liquid electrolyte (solid red curve in Figure 4c). The carbon signal persists across the interface for less than 1 nm. When compared with standard references (solid black curves in Figure 4c), the carbon spectrum at the liquid−solid interface exhibits a peak around 297 eV, most likely corresponding to C−O single bonds. This signal was only present at the liquid−solid interface of the *operando*-frozen samples and absent everywhere in the control samples, in which the CO_2RR was performed under the same conditions, but the control samples were frozen after the micro-EC was rested for 1 min at the OCV with no applied bias. This suggests that the adsorbed species is transient and can only be captured by rapid and operando freezing with applied voltage on. We hypothesize that the C−O bond originates from the intermediates chemically absorbed on the catalyst surface during the CO_2RR. Furthermore, it is likely that the C−O species on the Cu surface attract electrons away from Cu atoms and create a single valence Cu state, which is

https://doi.org/10.1021/acs.nanolett.3c03000
Nano Lett. 2024, 24, 10409−10417

consistent with our previous analysis on the intermediate Cu oxidation state.

More interestingly, the existence of the C−O single bond peak in the EELS spectra provides clues about the identity of the intermediate adsorbed species. In particular, many possible species have been hypothesized to form on the Cu surface in various proposed mechanisms (Figure 4d).[50] Among these, configurations 4−6 mainly consist of C−O single bonds. However, the sixth configuration has strong C-metal bond which has not been detected from either Cu EELS or C EELS. Thus, our data here suggest that the species detected in this system mainly has the fourth and fifth configuration, which have been both recognized as important intermediate states to produce liquid fuels such as CH_3OH (4th configuration) and formic acid (5th configuration) in Cu-catalyzed CO_2RR.[50,51]

In summary, we have developed a methodology to *operando*-freeze metastable intermediate states for cryo-EM and cryo-STEM characterization, revealing the structural and chemical information at electrified liquid−solid interfaces at the nanometer level. We observe a faster morphological evolution of Cu nanocatalysts during the CO_2RR than in a previous *in situ* liquid cell TEM study, which is possibly due to the existence of CO_2 molecules at the catalyst-electrolyte interface. Using cryo-STEM-EELS, we discover the existence of a single valence Cu (+) state and C−O bonding at the catalyst-electrolyte interface within a sub1 nm layer. A combination of our methodology with the instrumental developments of electron microscopy will further open opportunities in understanding the intermediate states of Cu nanocatalyst during the CO_2RR. Although we use Cu electrochemical CO_2RR as an example to demonstrate *operando*-freezing capability of this method, the experiments described here can potentially be extended to other e-beam sensitive electrochemical systems, such as batteries and other evolution reactions such as oxygen or hydrogen evolution.

■ ASSOCIATED CONTENT

Supporting Information

The Supporting Information is available free of charge at https://pubs.acs.org/doi/10.1021/acs.nanolett.3c03000.

Experimental details, additional electrochemical tests (micro-EC), additional characterization (CryoEM, Cryo-STEM-EELS, Cryo-STEM-ADF), and digital image of the O_2 detector (PDF)

Video S1: Liquid electrolyte uniformly covering the surface of Cu nanocatalysts when applying voltage during electrochemical CO_2RR, due to the electrowetting phenomenon (MP4)

■ AUTHOR INFORMATION

Corresponding Authors

Yuzhang Li − *Department of Materials Science and Engineering, Stanford University, Stanford, California 94305, United States; Department of Chemical and Biomolecular Engineering, University of California Los Angeles, Los Angeles, California 90095, United States;* orcid.org/0000-0002-1502-7869; Email: yicui@stanford.edu

Yi Cui − *Department of Materials Science and Engineering, Stanford University, Stanford, California 94305, United States; Stanford Institute for Materials and Energy Sciences, SLAC National Accelerator Laboratory, Menlo Park, California 94025, United States;* orcid.org/0000-0002-6103-6352; Email: yuzhangli@ucla.edu

Authors

Yanbin Li − *Department of Materials Science and Engineering, Stanford University, Stanford, California 94305, United States*

Yunzhi Liu − *Department of Materials Science and Engineering, Stanford University, Stanford, California 94305, United States;* orcid.org/0000-0003-0524-4023

Zewen Zhang − *Department of Materials Science and Engineering, Stanford University, Stanford, California 94305, United States;* orcid.org/0000-0002-4909-4330

Weijiang Zhou − *Biophysics Program, School of Medicine, Stanford University, Stanford, California 94305, United States;* orcid.org/0000-0002-3258-6005

Jinwei Xu − *Department of Materials Science and Engineering, Stanford University, Stanford, California 94305, United States;* orcid.org/0000-0003-2185-362X

Yusheng Ye − *Department of Materials Science and Engineering, Stanford University, Stanford, California 94305, United States*

Yucan Peng − *Department of Materials Science and Engineering, Stanford University, Stanford, California 94305, United States*

Xin Xiao − *Department of Materials Science and Engineering, Stanford University, Stanford, California 94305, United States;* orcid.org/0000-0003-1098-9484

Wah Chiu − *Biophysics Program, School of Medicine and Department of Bioengineering, Stanford University, Stanford, California 94305, United States; Division of CryoEM and Bioimaging, SSRL, SLAC National Accelerator Laboratory, Menlo Park, California 94025, United States;* orcid.org/0000-0002-8910-3078

Robert Sinclair − *Department of Materials Science and Engineering, Stanford University, Stanford, California 94305, United States*

Complete contact information is available at: https://pubs.acs.org/10.1021/acs.nanolett.3c03000

Author Contributions

[¶]Yan.L. and Yun.L. contributed equally to this work. Yan.L., Yuz.L.and Y.C. conceived the project and designed the experiments. Yan.L. and Yun.L. built the operando-freezing apparatus together. Yan.L., J.X. and Y.W. performed materials synthesis. Yan.L., Yun.L. and W.Z carried out cryo-EM experiments, Z.Z. helped with the data characterizations. Yan.L., Yuz.L., and Y.C. cowrote the manuscript. All authors discussed the results and commented on the manuscript.

Notes

The authors declare no competing financial interest.

■ ACKNOWLEDGMENTS

Y.C. and W.C. acknowledge the CryoEM research support from the Department of Energy, Office of Basic Energy Sciences, Division of Materials Science and Engineering under contract DE-AC02-76SF00515. Z.Z acknowledges support by Stanford Interdisciplinary Graduate Fellowship. Yuz. L. acknowledges support by the U.S. Department of Energy, Office of Science, Office of Basic Energy Sciences, under Award Number DE-SC0022955. We acknowledge the use and support of the Stanford-SLAC CryoEM Facilities, the Stanford Nano Shared Facilities and the Stanford Nanofabrication Facility. Yun. L., and R.S. acknowledge the support from the Toyota Research Institute − Accelerated Materials Design and Discovery (TRI-AMDD) program (Stanford University).

https://doi.org/10.1021/acs.nanolett.3c03000
Nano Lett. 2024, 24, 10409−10417

REFERENCES

(1) Jouny, M.; Luc, W.; Jiao, F. General techno-economic analysis of CO_2 electrolysis systems. *Ind. Eng. Chem. Res.* **2018**, *57*, 2165−2177.
(2) Gu, J.; Hsu, C.-S.; Bai, L.; Chen, H. M.; Hu, X. Atomically dispersed Fe^{3+} sites catalyze efficient CO_2 electroreduction to CO. *Science* **2019**, *364*, 1091−1094.
(3) Zheng, X.; et al. Sulfur-modulated tin sites enable highly selective electrochemical reduction of CO_2 to formate. *Joule* **2017**, *1*, 794−805.
(4) Higgins, D.; Hahn, C.; Xiang, C.; Jaramillo, T. F.; Weber, A. Z. Gas-diffusion electrodes for carbon dioxide reduction: A new paradigm. *ACS Energy Letters* **2019**, *4*, 317−324.
(5) Wang, H.; et al. Synergistic enhancement of electrocatalytic CO_2 reduction to C_2 oxygenates at nitrogen-doped nanodiamonds/Cu interface. *Nature Nanotechnol.* **2020**, *15*, 131−137.
(6) Li, J.; et al. Efficient electrocatalytic CO_2 reduction on a three-phase interface. *Nature Catalysis* **2018**, *1*, 592−600.
(7) Gong, Q.; Ding, P.; Xu, M.; Zhu, X.; Wang, M.; Deng, J.; Ma, Q.; Han, N.; Zhu, Y.; Lu, J.; et al. Structural defects on converted bismuth oxide nanotubes enable highly active electrocatalysis of carbon dioxide reduction. *Nat. Commun.* **2019**, *10*, 1−10.
(8) Garcia de Arquer, F. P.; Bushuyev, O. S.; De Luna, P.; Dinh, C.-T.; Seifitokaldani, A.; Saidaminov, M. I.; Tan, C.-S.; Quan, L. N.; Proppe, A.; Kibria, M. G. 2D metal oxyhalide-derived catalysts for efficient CO_2 electroreduction. *Adv. Mater.* **2018**, *30*, 1802858.
(9) Fan, L.; Xia, C.; Zhu, P.; Lu, Y.; Wang, H. Electrochemical CO_2 reduction to high-concentration pure formic acid solutions in an all-solid-state reactor. *Nat. Commun.* **2020**, *11*, 3633.
(10) Seh, Z. W.; Kibsgaard, J.; Dickens, C. F.; Chorkendorff, I.; Nørskov, J. K.; Jaramillo, T. F. Combining theory and experiment in electrocatalysis: Insights into materials design. *Science* **2017**, *355*, aad4998.
(11) Xu, K. Electrolytes and interphases in Li-ion batteries and beyond. *Chem. Rev.* **2014**, *114*, 11503−11618.
(12) Sood, A.; et al. Electrochemical ion insertion from the atomic to the device scale. *Nature Reviews Materials* **2021**, *6*, 847−867.
(13) Bazant, M. Z.; Thornton, K.; Ajdari, A. Diffuse-charge dynamics in electrochemical systems. *Phys. Rev. E* **2004**, *70*, 021506.
(14) Bazant, M. Z. Theory of chemical kinetics and charge transfer based on nonequilibrium thermodynamics. *Accounts of chemical research* **2013**, *46*, 1144−1160.
(15) Alia, S. M.; et al. Activity and durability of iridium nanoparticles in the oxygen evolution reaction. *J. Electrochem. Soc.* **2016**, *163*, F3105.
(16) Cherevko, S.; Geiger, S.; Kasian, O.; Mingers, A.; Mayrhofer, K. J. Oxygen evolution activity and stability of iridium in acidic media. Part 2.−Electrochemically grown hydrous iridium oxide. *J. Electroanal. Chem.* **2016**, *774*, 102−110.
(17) Tang-Kong, R.; Chidsey, C. E.; McIntyre, P. C. Reversible Decay of Oxygen Evolution Activity of Iridium Catalysts. *J. Electrochem. Soc.* **2019**, *166*, H712.
(18) Lee, K.-K.; Park, K.; Lee, H.; Noh, Y.; Kossowska, D.; Kwak, K.; Cho, M. Ultrafast fluxional exchange dynamics in electrolyte solvation sheath of lithium ion battery. *Nat. Commun.* **2017**, *8*, 1−9.
(19) Scott, S. B.; et al. Absence of oxidized phases in Cu under CO reduction conditions. *ACS Energy Letters* **2019**, *4*, 803−804.
(20) Li, Y.; Huang, W.; Li, Y.; Chiu, W.; Cui, Y. Opportunities for Cryogenic Electron Microscopy in Materials Science and Nanoscience. *ACS Nano* **2020**, *14*, 9263−9276.
(21) Zhang, Z.; et al. Cryogenic electron microscopy for energy materials. *Acc. Chem. Res.* **2021**, *54*, 3505−3517.
(22) Li, Y.; et al. Atomic structure of sensitive battery materials and interfaces revealed by cryo−electron microscopy. *Science* **2017**, *358*, 506−510.
(23) Li, Y.; et al. Cryo-EM structures of atomic surfaces and host-guest chemistry in metal-organic frameworks. *Matter* **2019**, *1*, 428−438.
(24) Lim, J.; et al. Origin and hysteresis of lithium compositional spatiodynamics within battery primary particles. *Science* **2016**, *353*, 566−571.
(25) Li, Y.; et al. Unravelling Atomic Structure and Degradation Mechanisms of Organic-Inorganic Halide Perovskites by Cryo-EM. *Joule* **2019**, *3*, 2854−2866.
(26) Zhang, Z.; et al. Capturing the swelling of solid-electrolyte interphase in lithium metal batteries. *Science* **2022**, *375*, 66−70.
(27) Zachman, M. J.; Tu, Z.; Choudhury, S.; Archer, L. A.; Kourkoutis, L. F. Cryo-STEM mapping of solid−liquid interfaces and dendrites in lithium-metal batteries. *Nature* **2018**, *560*, 345−349.
(28) Wang, X.; et al. New insights on the structure of electrochemically deposited lithium metal and its solid electrolyte interphases via cryogenic TEM. *Nano Lett.* **2017**, *17*, 7606−7612.
(29) Dandey, V. P.; et al. Time-resolved cryo-EM using Spotiton. *Nat. Methods* **2020**, *17*, 897−900.
(30) Ren, D.; et al. Selective electrochemical reduction of carbon dioxide to ethylene and ethanol on copper (I) oxide catalysts. *ACS Catal.* **2015**, *5*, 2814−2821.
(31) Li, C. W.; Kanan, M. W. CO_2 reduction at low overpotential on Cu electrodes resulting from the reduction of thick Cu_2O films. *J. Am. Chem. Soc.* **2012**, *134*, 7231−7234.
(32) Eilert, A.; et al. Subsurface oxygen in oxide-derived copper electrocatalysts for carbon dioxide reduction. *journal of physical chemistry letters* **2017**, *8*, 285−290.
(33) Mistry, H.; Varela, A. S.; Bonifacio, C. S.; Zegkinoglou, I.; Sinev, I.; Choi, Y.-W.; Kisslinger, K.; Stach, E. A.; Yang, J. C.; Strasser, P.; Cuenya, B. R. Highly selective plasma-activated copper catalysts for carbon dioxide reduction to ethylene. *Nat. Commun.* **2016**, *7*, 1−9.
(34) Bagger, A.; Ju, W.; Varela, A. S.; Strasser, P.; Rossmeisl, J. Electrochemical CO_2 reduction: a classification problem. *ChemPhysChem* **2017**, *18*, 3266−3273.
(35) Platzman, I.; Brener, R.; Haick, H.; Tannenbaum, R. Oxidation of polycrystalline copper thin films at ambient conditions. *J. Phys. Chem. C* **2008**, *112*, 1101−1108.
(36) Lum, Y.; Ager, J. W. Stability of residual oxides in oxide-derived copper catalysts for electrochemical CO_2 reduction investigated with ^{18}O labeling. *Angew. Chem., Int. Ed.* **2018**, *57*, 551−554.
(37) Yu, F.; Zhou, H.; Huang, Y.; Sun, J.; Qin, F.; Bao, J.; Goddard, W. A.; Chen, S.; Ren, Z. High-performance bifunctional porous non-noble metal phosphide catalyst for overall water splitting. *Nat. Commun.* **2018**, *9*, 1−9.
(38) Aran-Ais, R. M.; Rizo, R.; Grosse, P.; Algara-Siller, G.; Dembele, K.; Plodinec, M.; Lunkenbein, T.; Chee, S. W.; Cuenya, B. R. Imaging electrochemically synthesized Cu_2O cubes and their morphological evolution under conditions relevant to CO_2 electroreduction. *Nat. Commun.* **2020**, *11*, 1−8.
(39) Egerton, R. Radiation damage to organic and inorganic specimens in the TEM. *Micron* **2019**, *119*, 72−87.
(40) Mugele, F.; Baret, J.-C. Electrowetting: from basics to applications. *J. Phys.: Condens. Matter* **2005**, *17*, R705.
(41) Grassucci, R. A.; Taylor, D. J.; Frank, J. Preparation of macromolecular complexes for cryo-electron microscopy. *Nature protocols* **2007**, *2*, 3239−3246.
(42) Brüggeller, P.; Mayer, E. Complete vitrification in pure liquid water and dilute aqueous solutions. *Nature* **1980**, *288*, 569−571.
(43) Bammes, B. E.; Jakana, J.; Schmid, M. F.; Chiu, W. Radiation damage effects at four specimen temperatures from 4 to 100K. *J. Struct. Biol.* **2010**, *169*, 331−341.
(44) Grosse, P.; et al. Dynamic changes in the structure, chemical state and catalytic selectivity of Cu nanocubes during CO_2 electroreduction: size and support effects. *Angew. Chem., Int. Ed.* **2018**, *57*, 6192−6197.
(45) Reske, R.; Mistry, H.; Behafarid, F.; Roldan Cuenya, B.; Strasser, P. Particle size effects in the catalytic electroreduction of CO_2 on Cu nanoparticles. *J. Am. Chem. Soc.* **2014**, *136*, 6978−6986.
(46) Kim, D.; Kley, C. S.; Li, Y.; Yang, P. Copper nanoparticle ensembles for selective electroreduction of CO_2 to C_2−C_3 products. *Proceedings of the National Academy of Sciences* **2017**, *114*, 10560−10565.
(47) Huang, J.; Hormann, N.; Oveisi, E.; Loiudice, A.; De Gregorio, G. L.; Andreussi, O.; Marzari, N.; Buonsanti, R. Potential-induced

https://doi.org/10.1021/acs.nanolett.3c03000
Nano Lett. 2024, 24, 10409−10417

nanoclustering of metallic catalysts during electrochemical CO_2 reduction. *Nat. Commun.* **2018**, *9*, 1−9.
(48) De Luna, P.; et al. Catalyst electro-redeposition controls morphology and oxidation state for selective carbon dioxide reduction. *Nature Catalysis* **2018**, *1*, 103−110.
(49) EELS Info. Atlas of Carbon. https://eels.info/atlas/carbon (accessed July 25, 2022).
(50) Kortlever, R.; Shen, J.; Schouten, K. J. P.; Calle-Vallejo, F.; Koper, M. T. Catalysts and reaction pathways for the electrochemical reduction of carbon dioxide. *journal of physical chemistry letters* **2015**, *6*, 4073−4082.
(51) Zheng, T.; et al. Copper-catalysed exclusive CO_2 to pure formic acid conversion via single-atom alloying. *Nat. Nanotechnol.* **2021**, *16*, 1386−1393.

https://doi.org/10.1021/acs.nanolett.3c03000
Nano Lett. 2024, 24, 10409−10417